

Communication: Unraveling the ^4He droplet-mediated soft-landing from *ab initio*-assisted and time-resolved density functional simulations: $\text{Au}@^4\text{He}_{300}/\text{TiO}_2(110)$

María Pilar de Lara-Castells,^{1,a)} Néstor F. Aguirre,^{1,b)} Hermann Stoll,²

Alexander O. Mitrushchenkov,³ David Mateo,^{4,c)} and Martí Pi⁴

¹*Instituto de Física Fundamental (C.S.I.C.), Serrano 123, E-28006 Madrid, Spain*

²*Institut für Theoretische Chemie, Universität Stuttgart, D-70550 Stuttgart, Germany*

³*Université Paris-Est, Laboratoire Modélisation et Simulation Multi Echelle, MSME UMR 8208 CNRS, 5 bd Descartes, 77454 Marne-la-Vallée, France*

⁴*Department ECM, Facultat de Física, and IN²UB, Universitat de Barcelona, Diagonal 645, E-08028 Barcelona, Spain*

(Received 4 February 2015; accepted 25 March 2015; published online 3 April 2015)

An *ab-initio*-based methodological scheme for He-surface interactions and zero-temperature time-dependent density functional theory for superfluid ^4He droplets motion are combined to follow the short-time collision dynamics of the $\text{Au}@^4\text{He}_{300}$ system with the $\text{TiO}_2(110)$ surface. This composite approach demonstrates the ^4He droplet-assisted sticking of the metal species to the surface at low landing energy (below 0.15 eV/atom), thus providing the first theoretical evidence of the experimentally observed ^4He droplet-mediated soft-landing deposition of metal nanoparticles on solid surfaces [Mozhayskiy *et al.*, J. Chem. Phys. **127**, 094701 (2007) and Loginov *et al.*, J. Phys. Chem. A **115**, 7199 (2011)]. © 2015 AIP Publishing LLC. [<http://dx.doi.org/10.1063/1.4916955>]

The ultra-cold ^4He droplet-assisted synthesis and deposition of embedded metal nanoparticles (NPs) on solid surfaces attract nowadays strong attention.^{1–9} Pioneering experimental studies carried out by Vilesov and collaborators¹ showed that, with temperatures below 0.4 K, superfluid ^4He droplets serve not only as a cryogenic fluid in which metal NPs are synthesized but also as carriers to solid surfaces. The experimentally demonstrated quantum vortex-guided confinement of embedded metal NPs in thin and elongated nanowires inside ^4He droplets^{3,5,7} and bulk ^4He ¹⁰ has provided a renewed impetus owing to the special electro-, magneto-optical, and catalytic properties of the metal species so formed. The ^4He droplet-mediated technique has thus experienced a tremendous improvement and it is now possible to produce one-dimensional NPs with core-shell morphologies and different compositions^{5,6} and to create metal cluster-based films beyond the submonolayer regime⁸ in pre-active states.⁹

One of the most striking advantages of the ^4He droplet-assisted deposition is the possibility of so-called soft-landing (SL) conditions (see, e.g., Ref. 11 for a recent review). These conditions are characterized by sticking probabilities of the metal NPs close to 100% at the impact point with landing energies well below typical cohesive energies of the metal species (e.g., 3.8 eV/atom for gold¹²), thus avoiding that their restructuring alters the special physical and chemical NPs properties. The first successful SL experiments were realized by Cooks and collaborators¹³ using low-energy ion beams. The

SL deposition of metal NPs embedded in ^4He droplets was also inferred in the earliest experimental studies of Vilesov's group by proving that the size of deposited metal NPs agreed well with the estimated initial NPs sizes.² The assumption of SL deposition allowed to interpret the presence of elongated metal wires after deposition (outside the ^4He droplet) as a signature of the occurrence of quantum vortices inside the droplets by the same authors.³ Very recently, images of doped ^4He droplets by diffractive x-ray spectroscopy have made possible to confirm the existence of quantum vorticity.¹⁴ Experimental evidences of SL deposition have been also provided by Ernst's^{4,5} group, supporting them with molecular dynamics simulations,¹⁵ and by Ellis's⁷ group.

Despite the rapid growth of this research area, direct theoretical evidences for the SL deposition of embedded species with inclusion of the doped ^4He droplet dynamics have not been provided yet. The time-dependent density functional (TDDFT) method¹⁶ has been shown to be ideally suited to address the zero temperature dynamics of medium-sized droplets (~ 300 ^4He atoms) colliding with solid surfaces.^{17,18} Earlier TDDFT simulations on the collision of undoped ^4He drops¹⁷ indicated that the droplet spreading upon impact might cushion the deposition of an embedded species. The comparison with classical trajectory (CT) calculations predicting the splashing of the ^4He drop at impact¹⁷ demonstrated the key role of quantum He–He interaction effects. The details of ^4He droplet spreading mechanism have been very recently characterized through dispersion-accounting and dispersionless TDDFT simulations on a graphene sheet,¹⁸ highlighting the importance of an accurate description of the He-surface interaction. The combination of the dispersionless density functional dIDF developed by Pernal *et al.*,¹⁹ including periodic conditions, with high-level *ab initio* calculations on

^{a)}Author to whom correspondence should be addressed. Electronic mail: Pilar.deLara.Castells@csic.es

^{b)}Present address: Departamento de Química, Universidad Autónoma de Madrid, 28049 Madrid, Spain.

^{c)}Present address: Department of Chemistry and Biochemistry, California State University at Northridge, California 91330, USA.

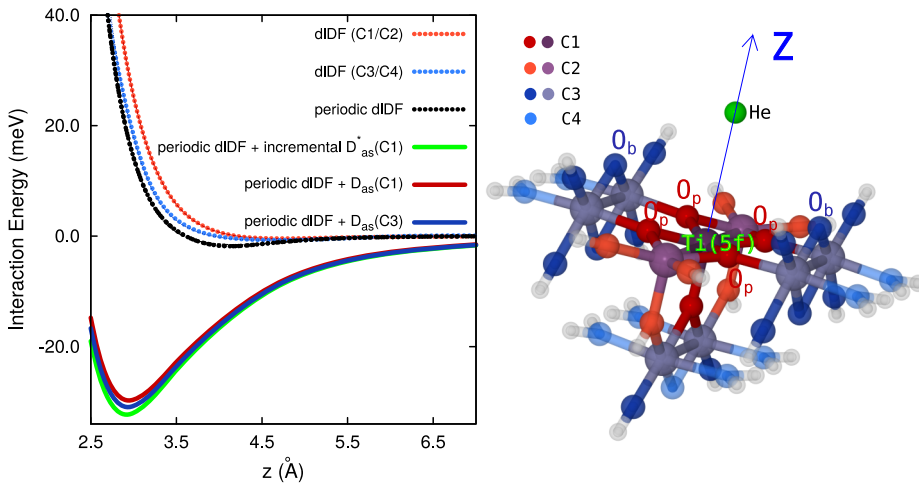


FIG. 1. Figure illustrating the hydrogen-saturated clusters chosen to model the $\text{TiO}_2(110)$ surface. The interaction energies obtained with the dI DF and periodic dI DF + incremental D_{as}^*/D_{as} approaches are also shown along with the clusters used for dI DF and D_{as} parametrizations. The He atom is located on top of the most stable site. The main interaction region comprises the He and the central Ti(5f) atoms along with the adjacent in-plane and bridging O atoms (denoted as O_p and O_b).

clusters for the dispersion has been proven to be an efficient approach to calculate accurate He-surface interactions.¹⁸ This technique together with the TDDFT method is applied here to prove ^4He droplet assisted SL deposition. As already anticipated,¹⁷ we have chosen the rutile TiO_2 (110) surface and a single gold atom as the embedded metal species. TiO_2 is a prototype transition metal-oxide with well-known applications as catalyst and photocatalyst,^{20,21} more recently in form of novel graphene- TiO_2 -based composites.²² Due to their optical properties, noble metal's NPs (Ag, Au) have seen more extensive use as the embedded NPs in experimental measurements.^{3–6}

In this work, we consider the short-time collision dynamics of the $\text{Au}@^4\text{He}_{300}$ droplet complex. Due to the high velocity of the system (~ 200 m/s in the experiment³) and the ^4He droplet size (diameter of ~ 23 Å), the collision is influenced by both short- and long-range regions of the He-surface interaction.¹⁷ It is thus important to account for short- and long-ranged electronic correlation effects. Applying the approach proposed in Ref. 18, the total interaction energy $E_{\text{int}}^{\text{total}}$ of the He-surface system is expressed as

$$E_{\text{int}}^{\text{total}} = E_{\text{int}}^{\text{HF}} + E_{\text{int}}^{\text{intra-corr}} + E_{\text{int}}^{\text{inter-corr}}, \quad (1)$$

where $E_{\text{int}}^{\text{HF}}$, the Hartree-Fock (HF) interaction energy, is calculated using the periodic slab model to account for long-ranged induction effects. The *intramonomer* correlation contribution ($E_{\text{int}}^{\text{intra-corr}}$) can be estimated as the difference between HF interaction energies and those calculated with the dispersionless functional dI DF.¹⁹ Both $E_{\text{int}}^{\text{HF}}$ and $E_{\text{int}}^{\text{intra-corr}}$ terms are included in the periodic dI DF approach.¹⁸ As a benchmark, the method of increments proposed by Stoll²³ is applied to extract the most important *intramonomer* correlation contribution using the coupled cluster treatment with singles and double excitations and perturbative triples [CCSD(T)] and surface cluster models. Applying this method,^{23–25} the correlation energy is expressed as a cumulant expansion in units of localized orbital groups (LOGs) centered at the adsorbate and the surface, which define n -body increments (n denote the number of interacting LOGs within each increment). The *intermonomer* correlation contribution ($E_{\text{int}}^{\text{inter-corr}}$) is identified with the dispersion contribution, fitted by means of the effective pairwise D_{as} functional of Szalewicz and

collaborators,^{26,27} and then computed for the extended system. The calculation of $E_{\text{int}}^{\text{total}}$ is then reduced to

$$E_{\text{int}}^{\text{total}} = E_{\text{int}}^{\text{dI DF}} - \sum_{X \in \text{surface}} \sum_n \frac{\sqrt{C_n^{\text{He}} C_n^X}}{R_{\text{HeX}}^n} f_n(\sqrt{\beta_{\text{He}} \beta_X} R_{\text{HeX}}),$$

where f_n ($n = 6, 8$) are damping functions.²⁸ The parameters of the functional have been fitted to CCSD(T) *intermonomer* correlation contributions evaluated using the method of increments (incremental D_{as}^* approach). As proposed in the original dI DF + D_{as} approach,^{19,26,27} the D_{as} functional has been also parametrized by calculating dispersion energies with symmetry adapted perturbation theory (SAPT) and DFT-based descriptions of the adsorbate and the surface clusters, the SAPT(DFT) approach.^{29,30} The TiO_2 (110) surface was modeled with the clusters shown in Figure 1. We used the computational setups reported in Refs. 31 and 32 (see also supplementary material³³). Cluster and periodic calculations were performed with the MOLPRO³⁴ and CRYSTAL14³⁵ packages including the published dI DF implementations.^{18,31} The method of increments was applied using the augmented polarized correlation-consistent double- and triple- ζ basis sets of Dunning and collaborators.³⁶ Table I collects the values of the different interaction energy contributions. From Fig. 1, we can notice how the dispersionless interaction energies from cluster dI DF calculations approach the periodic counterpart upon expanding the cluster model. The estimated $E_{\text{int}}^{\text{intra-corr}}$ values attain convergence already for the C_3 cluster. The *intramonomer* correlation term has an attractive long-range tail but becomes repulsive at short-range and grows exponentially upon decreasing the He-surface distance (see Table I). Repulsion is due to the correlation space truncation exerted by the He atom LOG^{23,25,31} and it is influenced by the local chemical environment of the nearby O_p atoms. What is important to notice is that the periodic dispersionless dI DF approach provides accurate *intramonomer* correlation estimations (see Table I). On the other hand, the *intermonomer* correlation is identified with the dispersion contribution, as reflected in Table I by the similar values provided by the D_{as} parametrizations using the method of increments (the incremental D_{as}^* scheme¹⁸) and the SAPT(DFT) treatment (D_{as}^* approach²⁶). Despite being long-ranged, the dispersion

TABLE I. Contributions to the He-TiO₂ (110) interaction energy as a function of distance from the He atom to the Ti(5f) adsorption site. (a) Best estimation *via* the method of increments with the one- and two-body contributions calculated at CCSD(T) and second-order Möller-Plesset perturbation (MP2) levels of theory, respectively.³³ (b) Ref. 31.

Z (Å)	2.6	3.0	3.4	3.8	4.5	6.0	8.0
Energy/meV							
$E_{\text{int}}^{\text{HF}}/\text{slab}$	20.7	4.6	-0.2	-1.0	-0.6	-0.1	0
$E_{\text{int}}^{\text{intra-corr}}$	Method of increments/dispersionless						
CCSD(T)/C ₃ ^(a)	24.7	8.1	2.3	0.5	-0.8	-1.1	-0.6
	Periodic dLDF/dispersionless						
dLDF/slab	31.0	9.6	2.5	-0.2	-0.8	0.0	0
$E_{\text{int}}^{\text{inter-corr}}$	D _{as} parametrization/dispersion						
SAPT(DFT)/C ₁ ^(b)	-83.3	-48.6	-29.8	-19.2	-9.8	-3.1	-1.0
SAPT(DFT)/C ₃	-79.1	-46.7	-28.3	-18.7	-9.6	-3.1	-1.0
$E_{\text{int}}^{\text{inter-corr}}$	Incremental D _{as} [*] parametrization/dispersion						
CCSD(T)/C ₁	-81.6	-47.7	-29.3	-23.4	-9.6	-3.1	-1.0
$E_{\text{int}}^{\text{tot}}$	-27.4	-32.5	-26.0	-18.9	-11.0	-3.2	-1.0

energy contribution is less dependent on the chemical environment than the dispersionless counterpart so that the D_{as} parametrizations using C₁ and C₃ clusters provide energies differing by less than 3% on average (see Table I).³³

To perform the dynamical simulations with the TDDFT method, the He-TiO₂(110) interaction was averaged by considering 15 adsorption sites (see supplementary material³³). The details of the method when applied to the collision dynamics with solid surfaces can be found in Ref. 17. Due to its large mass, the solvated Au atom is described as a classical particle with position $\mathbf{r}_{\text{Au}}(t)$ (see, e.g., Ref. 37) while the helium solvent is described by an effective complex wavefunction $\Psi(\mathbf{r}, t)$ such that $\rho(\mathbf{r}, t) = |\Psi(\mathbf{r}, t)|^2$. The ⁴He₃₀₀ drop follows the 3D time-dependent equation,

$$\frac{\partial \Psi(\mathbf{r}, t)}{\partial t} = -\frac{(t + \Lambda(\mathbf{r}))}{\hbar} \left\{ -\frac{\hbar^2}{2m_{\text{He}}} \Delta + \frac{\delta \mathcal{E}_{\text{He}}[\rho]}{\delta \rho(\mathbf{r})} \right\} \Psi(\mathbf{r}, t) - \frac{i}{\hbar} \left\{ V_{\text{ext}}^{\text{He-surface}}(z) - V_{\text{ext}}^{\text{He-Au}}(|\mathbf{r} - \mathbf{r}_{\text{Au}}|) \right\} \Psi(\mathbf{r}, t),$$

where $\mathcal{E}_{\text{He}}[\rho]$ is a modification³⁸ of the Orsay-Trento density functional³⁹ capable of describing the very structured helium configurations appearing during the collision.¹⁸ The terms $V_{\text{ext}}^{\text{He-Au}}$ and $V_{\text{ext}}^{\text{He-surface}}$ denote the He-Au and He-surface pair potentials, respectively, and $\Lambda(\mathbf{r})$ is a damping function avoiding the reflection on the box boundaries. This equation is coupled to that for the Au atom,

$$m_{\text{Au}} \ddot{\mathbf{r}}_{\text{Au}} = - \left[\int d\mathbf{r} (\nabla_{\mathbf{r}} \rho(\mathbf{r})) V_{\text{ext}}^{\text{He-Au}}(|\mathbf{r} - \mathbf{r}_{\text{Au}}|) \right] - \nabla_{\mathbf{r}_{\text{Au}}} [V_{\text{ext}}^{\text{Au-surface}}(z)],$$

where $V_{\text{ext}}^{\text{Au-surface}}$ is the Au-surface potential with Au on the hollow site, having a well-depth of ~400 meV (at ~2.8 Å). This interaction was calculated by following the study of Chrétien and Metiu⁴⁰ and considering nine adsorption sites.³³ We employed the He-Au pair potential calculated at CCSD(T) level by Tong *et al.*⁴¹ The initial configuration

of the Au@⁴He₃₀₀ complex is obtained via DF calculations without including the droplet-surface interaction. Since the He-Au interaction strength (~1.9 meV at ~4 Å) is larger than the He-He pair interaction (~1 meV), the Au atom locates at the droplet center with the closest helium solvation shell at about 4.5 Å. The dynamical simulation starts with the Au@⁴He₃₀₀ droplet mass center at 27.4 Å from the surface. Following the experimental setup, the Au-droplet complex is provided with an initial velocity towards the surface of 200 m/s. Figure 2 shows the ⁴He₃₀₀ system evolution during the first 20 ps (Multimedia view). The Au atom and ⁴He₃₀₀ mass center motions can be followed from Figure 3 in terms of the position and acceleration along the surface normal as a function of time. The averaged positions from CT calculations of the full Au@⁴He₃₀₀ system are also shown.³³

The He-surface dispersion interaction (see Table I) causes an early compression of the ⁴He droplet while moving towards the surface during the first 5 ps (see Fig. 2 and Multimedia view). Owing to the attractive He-Au interaction, the Au atom adjusts its position to the compressed helium droplet and it is accelerated towards the rutile substrate at $t = 5$ ps (see Fig. 3). This initial acceleration and decoupling from the droplet-mass-center motion of the Au atom are followed by the pronounced deformations in the nearest helium solvation shell, as reflected in its flattening and appearance of high density fluctuations at $t = 6$ ps (see Fig. 2). Due to the short-ranged Au-He repulsion, the impurity is accelerated in the opposite direction (backwards) upon the interaction with high-density helium features, as a result of which the desorption of helium atoms can be appreciated (see Fig. 2). One picosecond later, at $t = 7$ ps (see Fig. 2), a solid-like helium spot can be seen on top of the Au atom as well as the emission of pressure density waves propagating backwards from the surface. Solid-like helium structures do appear upon the bending of helium density waves travelling towards the middle of the surface plane due the dispersion

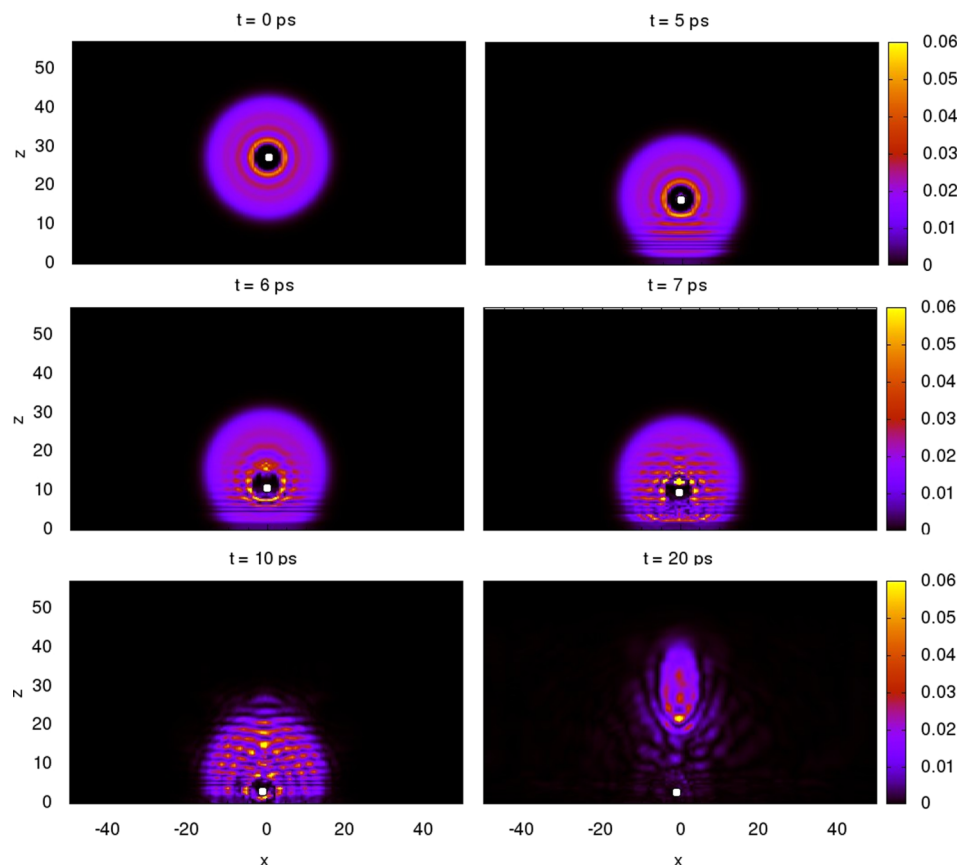


FIG. 2. Snapshots showing the time evolution of the Au@ $^4\text{He}_{300}$ droplet at impact with the solid surface. The z axis (in Å) is oriented at the surface normal direction. The density values (in Å $^{-3}$) are given in the legends. (Multimedia view) [URL: <http://dx.doi.org/10.1063/1.4916955.1>]

component of the He–Au and He–surface interactions.¹⁸ These high density helium configurations are not stable and become annihilated upon the impact with either the Au atom or the surface (see Fig. 2, Multimedia view). The Au atom thus oscillates back and forth by following the dynamical ^4He droplet structural changes, leading to further symmetry breaking effects and rearrangements of the closest helium solvation shell. Eventually, after being accelerated towards the surface at $t = 8$ ps (see Fig. 2), the Au atom gets close enough to the rutile surface for becoming trapped in the minimum of the Au–surface potential at $t = 10$ ps (see Figs. 2 and 3). As reflected in the Au atom deceleration just before the sticking (see Fig. 3), the impact is cushioned by the helium layer above the surface plane. After 10 ps, the impurity keeps oscillating about the minimum of the potential until the end of the simulation, with the acceleration along the surface normal averaging to zero (see Fig. 3). Immediately after the Au atom trapping, the evaporation-like process of He atoms along the surface normal becomes more pronounced and clearly evident at $t = 20$ ps (see Fig. 2). This is also reflected in the recoil of the droplet mass center position backwards from the surface (see Fig. 3). Although being much more diffuse than for undoped $^4\text{He}_{300}$ droplets, the spreading is very pronounced also for the doped Au@ $^4\text{He}_{300}$ droplet. Thus, at $t = 10$ ps (20 ps), 24% (70%) of the He atoms have spread and evaporated along the surface plane. The evaporation-like process is favored as compared with the undoped case because of the energy transfer each time that the impurity impacts the nearby ^4He droplet surface.

After the sticking, the kinetic energy associated to the Au atom motion along the surface normal drops to values

well below 0.1 eV. Although some lateral motion along the surface plane can be observed (Fig. 2, Multimedia view), the total kinetic energy stays below 0.15 eV during the last picoseconds of the simulation. Since this value is much

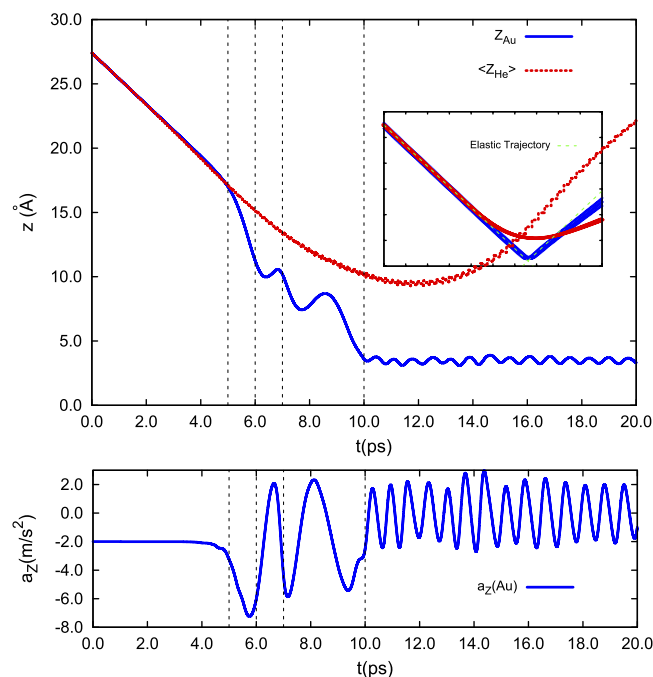


FIG. 3. Upper panel: position of the Au atom and the helium droplet mass center with respect to the rutile surface plane. The inset shows the averaged positions from CT calculations. Lower panel: acceleration component of the Au atom along the surface normal. The vertical dashed lines indicate the times associated to the snapshots in Fig. 2.

smaller than the cohesive energy of gold clusters and bulk gold (~ 2.1 and 3.8 eV/atom^{12,42}), it can be concluded that the conditions characterizing a soft-landing process¹¹ are satisfied. Comparing the results obtained through TDDFT and CT calculations (see Fig. 3), it becomes even more evident that the ^4He droplet-assisted sticking is a process driven by the density fluctuations of a quantum fluid: there is no sticking but only a slight deviation from an elastic trajectory of the Au atom when the helium drop is described classically. However, the classical picture provides insights into the time scales of the ^4He droplet collective motion and, in particular, the droplet rebound after the Au atom impact (see Fig. 3). Interestingly, trapped trajectories appear upon decreasing the impact velocity and increasing the droplet size.³³ The initial velocity decrease is expected to slow down the soft-landing process when the TDDFT formulation is applied.³³ Molecular dynamics simulations could assist the zero-temperature TDDFT description in yielding the time scales for the thermalization with room temperature surfaces. Although the metal atom trapping is too fast for the low frequency (surface) phonon modes to prevent it, it is clear that they might promote the diffusion and aggregation of the soft-landed metal species. As the calculated surface relaxations caused by helium are found to be small, the thermal surface vibrations are expected to affect the helium drop dynamics after the soft-landing process is finished (i.e., 10 ps).

In concluding, the present work has clearly evidenced the soft, ^4He droplet-assisted, deposition of an embedded noble metal species onto a solid surface, providing theoretical support to the experimental measurements with the newly developed deposition technique. It has been also shown that the sticking process is very fast (~ 10 ps) and that the quantum density fluctuations upon the interaction of the ^4He drop with the surface, as well as that of the Au atom itself with its nearby solvation shell, play a crucial role in assisting it. In contrast, the inclusion of the long-range dispersion in the Au-surface potential leaves the soft-landing process almost unmodified.³³ Since the helium density fluctuations are much influenced by the specific He-surface potential, the well established accuracy of the periodic d1DF + D_{as} /incremental D_{as}^* approaches¹⁸ for the He-surface interaction is considered to be highly relevant. The combination of this approach with the TDDFT method thus opens the way for further first-principles simulations of the short-time ^4He droplet-assisted deposition dynamics. Complementary molecular dynamics simulations could provide insights into the influence of phonon-mediated surface effects at longer time scales upon the collision with room temperature surfaces.

We thank Andrey Vilesov and Krzysztof Szalewicz for very useful suggestions and discussions. This work has been supported by Grant Nos. CCG08-CSIC/ESP-3680 from CSIC-CM, FIS2011-29596-C02-01 and FIS2011-28617-C02-01 from DGI, Spain (FEDER), and 2009SGR1289 from Generalitat de Catalunya. The support of COST Action CM1405 “Molecules in Motion (MOLIM)” is also acknowledged. The Cesga Super-Computer Center (Galicia) and the Centro Técnico de Informática (CTI, CSIC) are acknowledged for allocating computer time.

- ¹V. Mozhayskiy, M. N. Slipchenko, V. K. Adamchuk, and A. F. Vilesov, *J. Chem. Phys.* **127**, 094701 (2007).
- ²E. Loginov, L. F. Gómez, and A. F. Vilesov, *J. Phys. Chem. A* **115**, 7199 (2011).
- ³L. F. Gómez, E. Loginov, and A. F. Vilesov, *Phys. Rev. Lett.* **108**, 155302 (2012).
- ⁴A. Volk, P. Thaler, M. Koch, E. Fisslthaler, W. Grogger, and W. E. Ernst, *J. Chem. Phys.* **138**, 214312 (2013).
- ⁵P. Thaler, A. Volk, F. Lackner, J. Steurer, D. Knez, W. Grogger, F. Hofer, and W. E. Ernst, *Phys. Rev. B* **90**, 155442 (2014).
- ⁶S. Yang, A. M. Ellis, D. Spence, C. Feng, A. Boatwright, E. Latimer, and C. Binns, *Nanoscale* **5**, 11545 (2013).
- ⁷D. Spence, E. Latimer, C. Feng, A. Boatwright, A. Ellis, and S. Yang, *Phys. Chem. Chem. Phys.* **16**, 6903 (2014).
- ⁸S. B. Emery, K. B. Rider, B. K. Little, A. M. Schrand, and C. M. Lindsay, *J. Chem. Phys.* **139**, 044307 (2013).
- ⁹S. B. Emery, K. B. Rider, and C. M. Lindsay, *Propellants, Explos., Pyrotech.* **39**, 161 (2014).
- ¹⁰E. Gordon, A. Karabulin, V. Matyushenko, V. Sizov, and I. Sinov, *Phys. Chem. Chem. Phys.* **16**, 25229 (2014).
- ¹¹V. N. Popok, I. Barke, E. E. B. Campbell, and K.-H. Meiwes-Broer, *Surf. Sci. Rep.* **66**, 347 (2011).
- ¹²C. Kittel, *Introduction to Solid State Physics*, 8th ed. (John Wiley and Sons, Hoboken, NJ, 1934), p. 50.
- ¹³S. A. Miller, H. Luo, S. J. Pachuta, and R. G. Cooks, *Science* **275**, 1447 (1997).
- ¹⁴L. F. Gómez *et al.*, *Science* **345**, 906 (2014).
- ¹⁵P. Thaler, A. Volk, M. Ratschek, M. Koch, and W. E. Ernst, *J. Chem. Phys.* **140**, 044326 (2014).
- ¹⁶D. Mateo, D. Jin, M. Barranco, and M. Pi, *J. Chem. Phys.* **134**, 044507 (2011).
- ¹⁷N. F. Aguirre, D. Mateo, A. O. Mitrushchenkov, M. Pi, and M. P. de Lara-Castells, *J. Chem. Phys.* **136**, 124703 (2012).
- ¹⁸M. P. de Lara-Castells, H. Stoll, B. Civalieri, M. Causà, E. Voloshina, A. O. Mitrushchenkov, and M. Pi, *J. Chem. Phys.* **141**, 151102 (2014).
- ¹⁹K. Pernal, R. Podeszwa, K. Patkowski, and K. Szalewicz, *Phys. Rev. Lett.* **103**, 263201 (2009).
- ²⁰U. Diebold, *Surf. Sci. Rep.* **48**, 53 (2003).
- ²¹T. L. Thomson and J. T. Yates, Jr., *Chem. Rev.* **106**, 4428 (2006).
- ²²M.-Q. Yang, N. Zhang, M. Pagliaro, and Y.-J. Xu, *Chem. Soc. Rev.* **43**, 8240 (2014).
- ²³H. Stoll, *J. Chem. Phys.* **97**, 8449 (1992).
- ²⁴B. Paulus, *Phys. Rep.* **428**, 1 (2006).
- ²⁵V. Staemmler, *J. Phys. Chem. A* **115**, 7153 (2011).
- ²⁶R. Podeszwa and K. Szalewicz, *J. Chem. Phys.* **136**, 161102 (2012).
- ²⁷R. Podeszwa, K. Pernal, K. Patkowski, and K. Szalewicz, *J. Phys. Chem. Lett.* **1**, 550 (2010).
- ²⁸K. T. Tang and J. P. Toennies, *J. Chem. Phys.* **80**, 3726 (1984).
- ²⁹A. J. Misquitta, B. Jezierski, and K. Szalewicz, *Phys. Rev. Lett.* **91**, 033201 (2003).
- ³⁰A. Hesselmann and G. Jansen, *Chem. Phys. Lett.* **367**, 778 (2003).
- ³¹M. P. de Lara-Castells, H. Stoll, and A. O. Mitrushchenkov, *J. Phys. Chem. A* **118**, 6367 (2014).
- ³²M. P. de Lara-Castells, N. F. Aguirre, and A. O. Mitrushchenkov, *Chem. Phys.* **399**, 272 (2012).
- ³³See supplementary material at <http://dx.doi.org/10.1063/1.4916955> for additional material on the electronic structure and dynamical calculations as well as Fig. 2, Multimedia view.
- ³⁴H.-J. Werner, P. J. Knowles, G. Knizia, F. R. Manby, M. Schütz, P. Celani, T. Korona, R. Lindh, A. O. Mitrushchenkov, G. Rauhut *et al.*, *MOLPRO*, version 2012.1, a package of *ab initio* programs, 2012, see <http://www.molpro.net>.
- ³⁵R. Dovesi, V. R. Saunders, C. Roetti, R. Orlando, C. M. Zicovich-Wilson, F. Pascale, B. Civalieri, K. Doll, N. M. Harrison, I. J. Bush, P. D’Arco, M. Llunel, M. Causà, and Y. Noël, *CRYSTAL14 User’s Manual*, Università Torino, Torino, 2014, <http://www.crystal.unito.it>.
- ³⁶D. E. Woon and T. H. Dunning, Jr., *J. Chem. Phys.* **100**, 2975 (1994).
- ³⁷D. Mateo, A. Leal, A. Hernando, M. Barranco, M. Pi, F. Cargnoni, M. Mella, X. Zhang, and M. Drabbels, *J. Chem. Phys.* **140**, 131101 (2014).
- ³⁸F. Ancilotto, M. Barranco, F. Caupin, R. Mayol, and M. Pi, *Phys. Rev. B* **72**, 214522 (2005).
- ³⁹F. Dalfovo, A. Lastrì, L. Pricapenko, S. Stringari, and J. Treiner, *Phys. Rev. B* **52**, 1193 (1995).
- ⁴⁰S. Chrétien and H. Metiu, *J. Chem. Phys.* **127**, 084704 (2007).
- ⁴¹X.-F. Tong, C.-L. Yang, Y.-P. An, M.-S. Wand, X.-G. Ma, and D.-H. Wang, *J. Chem. Phys.* **131**, 244304 (2009).
- ⁴²B. Chan and W. L. Yim, *J. Chem. Theory Comput.* **9**, 1964 (2013).